

## MIT Open Access Articles

*Estimation of the bed shear stress in vegetated and bare channels with smooth beds*

The MIT Faculty has made this article openly available. **Please share** how this access benefits you. Your story matters.

**Citation:** Yang, Judy Q., Francois Kerger, and Heidi M. Nepf. "Estimation of the Bed Shear Stress in Vegetated and Bare Channels with Smooth Beds." *Water Resources Research* (May 2015): n/a–n/a.

**As Published:** <http://dx.doi.org/10.1002/2014WR016042>

**Publisher:** American Geophysical Union (Wiley platform)

**Persistent URL:** <http://hdl.handle.net/1721.1/97473>

**Version:** Author's final manuscript: final author's manuscript post peer review, without publisher's formatting or copy editing

**Terms of use:** Creative Commons Attribution-Noncommercial-Share Alike



**1 Estimation of the bed shear stress in vegetated and**  
**2 bare channels with smooth beds**

Judy Q. Yang,<sup>1</sup> Francois Kerger,<sup>1</sup> Heidi M. Nepf<sup>1</sup>

---

Corresponding author: Judy Qingjun Yang, Department of Civil and Environmental Engineering, Massachusetts Institute of Technology, 15 Vassar Street, Building 48-216D, Cambridge, MA 02139, USA. (qjyang@mit.edu)

<sup>1</sup>Department of Civil and Environmental Engineering, Massachusetts Institute of Technology, Cambridge, Massachusetts, USA

3 **Abstract.** The shear stress at the bed of a channel influences important  
4 benthic processes such as sediment transport. Several methods exist to es-  
5 timate the bed shear stress in bare channels without vegetation, but most  
6 of these are not appropriate for vegetated channels due to the impact of veg-  
7 etation on the velocity profile and turbulence production. This study pro-  
8 poses a new model to estimate the bed shear stress in both vegetated and  
9 bare channels with smooth beds. The model, which is supported by measure-  
10 ments, indicates that for both bare and vegetated channels with smooth beds,  
11 within a viscous sub-layer at the bed, the viscous stress decreases linearly  
12 with increasing distance from the bed, resulting in a parabolic velocity pro-  
13 file at the bed. For bare channels, the model describes the velocity profile  
14 in the overlap region of the Law of the Wall. For emergent canopies of suf-  
15 ficient density (frontal area per unit canopy volume  $a \geq 4.3m^{-1}$ ), the  
16 thickness of the linear-stress layer is set by the stem diameter, leading to a  
17 simple estimate for bed shear stress.

## 1. Introduction

18 In aquatic systems, sediment transport plays a significant role in the function and mor-  
19 phology of hydraulic structures [*Robbins and Simon*, 1983; *Bennett et al.*, 2008; *García*,  
20 2008], the erosion and geomorphic evolution of coastal areas and channels [*Christiansen*  
21 *et al.*, 1981; *Shields et al.*, 1995; *Gacia and Duarte*, 2001; *Shields Jr et al.*, 2004], the tur-  
22 bidity of fish habitats [*Lenhart*, 2008; *Montakhab et al.*, 2012], and the fate of nutrients,  
23 organic matter and pollutants in channels [*Schulz et al.*, 2003; *Brookshire and Dwire*, 2003;  
24 *Schulz and Peall*, 2001]. To date, sediment transport in bare channels has been exten-  
25 sively investigated, and multiple empirical equations have been proposed to quantify the  
26 sediment transport rate in bare channels [e.g., *Yalin*, 2013; *Graf*, 1984]. Most of these  
27 equations relate the sediment transport rate to the shear stress at the bed,  $\tau_b$ , or the  
28 friction velocity  $U_* = \sqrt{\tau_b/\rho}$ , with fluid density  $\rho$  [e.g., *Biron et al.*, 2004; *Wilcock*, 1996].

29 Recently, increasing attention has turned to sediment transport in vegetated channels  
30 [e.g., *Jordanova and James*, 2003; *Kothyari et al.*, 2009; *Zong and Nepf*, 2010; *Montakhab*  
31 *et al.*, 2012]. Understanding the impact of vegetation on sediment transport is important  
32 because vegetation is a basic component of most natural water environments. In addition,  
33 vegetation has been widely used in river restoration both to create habitat and to reduce  
34 bank erosion [*Shields et al.*, 1995; *Inoue and Nakano*, 1998; *Abbe et al.*, 2003]. *Sand-*  
35 *Jensen* [1998] observed that streams with vegetation retained up to 80% of the sediment  
36 in transit downstream. Similarly, *Warren et al.* [2009] have shown that a vegetated reach  
37 retained 50% more corn pollen than an unvegetated reach of similar length. Despite the

38 important role vegetation plays in sediment transport, the impact of vegetation on the  
39 flow field and sediment transport is not yet fully understood.

40 Recent studies suggest that the sediment transport rate in vegetated channels may be  
41 related to the bed shear stress  $\tau_b$ , similar to bare channel flows [*Jordanova and James,*  
42 2003; *Kothyari et al., 2009*]. However, the typical methods used to estimate the bed shear  
43 stress, or the bed friction velocity ( $U_* = \sqrt{\tau_b/\rho}$ ), in a bare channel (listed below) are  
44 difficult or not appropriate in vegetated channels, in part because the stress acting on the  
45 bed ( $\tau_b$ ) is only a fraction of the total flow resistance. [*Biron et al., 2004; Rowiński and*  
46 *Kubrak, 2002*].

47 First, methods based on fitting the log law of the wall do not work because the mean  
48 velocity profile near the bed is not logarithmic for either submerged or emergent vegetation  
49 [*Kundu and Cohen, 2008; Nezu and Nakagawa, 1993; Nepf, 2012a; Liu et al., 2008*].

50 Second, the slope method used in bare channels is based on the balance of bed shear  
51 stress and the potential forcing due to the water surface slope, i.e.  $\tau_b = \rho g s H$ , in which  
52  $g$  is the gravitational acceleration,  $H$  is the water depth, and the potential gradient  $s$  is  
53 equal to the water surface slope, which for uniform flow is also the bed slope. In vegetated  
54 channels, the potential forcing  $\rho g s H$  balances both the bed shear stress and the vegetative  
55 drag. Some researchers have estimated the bed shear stress by subtracting the vegetative  
56 drag from the potential forcing [*Jordanova and James, 2003; Kothyari et al., 2009*]. This  
57 method is prone to large uncertainty, because both vegetative drag and the potential  
58 forcing are an order of magnitude larger than bed shear stress [*Jordanova and James,*  
59 2003; *Tanino and Nepf, 2008*].

60 Third, in bare channel flow, the bed shear stress can be estimated from the maximum  
61 near-bed Reynolds stress, or by extrapolating the linear profile of Reynolds stress to the  
62 bed [*Nezu and Rodi*, 1986]. However, within regions of vegetation the Reynolds stress  
63 profile does not increase linearly towards the bed, but rather has a vertical distribution  
64 that reflects the distribution of vegetation [*Nepf and Vivoni*, 2000]. It is therefore inap-  
65 propriate to apply the Reynolds stress method in vegetated channels.

66 Fourth, in a bare channel the near-bed turbulent kinetic energy (*TKE*) can be used  
67 to estimate the bed shear stress, because the *TKE* is predominantly generated by shear  
68 production at the bed, such that a link exists between the bed shear stress and *TKE*:  $\tau_b \approx$   
69  $0.2TKE$  [*Stapleton and Huntley*, 1995]. In vegetated channels, however, the turbulence  
70 generated by the vegetation dominates the total *TKE* [*Nepf and Vivoni*, 2000], so that  
71 there is no correlation between bed shear stress and turbulent kinetic energy [*Nepf*, 2012b].

72 Finally, in the case of smooth beds, the bed shear stress may be estimated directly using  
73 the velocity gradient at the bed. However, this involves the accurate measurement of the  
74 mean velocity profile within the viscous sub-layer, which is technically very difficult.

75 From the above list, we see that the estimation of bed shear stress in a vegetated channel  
76 remains a key limitation in the description of vegetated channel hydraulics. *Rowiński and*  
77 *Kubrak* [2002] proposed a mixing length model to predict the bed shear stress in a channel  
78 with emergent vegetation. However, their model requires iteration and does not have a  
79 practical form. In this paper, we propose a new model to estimate the bed shear stress in  
80 vegetated channels that has the same form in bare channels. It is important to note that  
81 our study only considers emergent vegetation, i.e. vegetation that fills the entire water  
82 column, and channels with smooth and impermeable beds. Therefore, this is only a first

83 step toward providing a parameterization that will work for field conditions. A discussion  
 84 on how this model may be extended in the future to channels with non-smooth beds can  
 85 be found in section 5.

## 2. Theory

### 2.1. Governing equations

86 To account for the spatial heterogeneity of the flow inside a canopy, time- and space-  
 87 averaged (double-averaged) Navier Stokes (N-S) equations [Nikora *et al.*, 2007, 2013] are  
 88 commonly employed in the study of both terrestrial canopies [Finnigan, 2000; Raupach  
 89 and Shaw, 1982] and aquatic vegetated canopies [López and García, 2001; Luhar *et al.*,  
 90 2008]. We refer the interested readers to Nikora *et al.* [2007, 2013] for details about the  
 91 double-averaging method. The double-averaged N-S equations in an emergent canopy of  
 92 uniform porosity are:

$$\frac{\partial \langle \bar{u}_i \rangle}{\partial x_i} = 0 \quad (1)$$

$$\frac{\partial \langle \bar{u}_i \rangle}{\partial t} + \langle \bar{u}_j \rangle \frac{\partial \langle \bar{u}_i \rangle}{\partial x_j} = g_i - \frac{1}{\rho} \frac{\partial \langle \bar{p} \rangle}{\partial x_i} + \frac{1}{\rho} \frac{\partial}{\partial x_j} \left( \tau_{ij}^{disp} + \langle \tau_{ij}^{Rey} \rangle + \langle \tau_{ij}^{vis} \rangle \right) - D_i \quad (2)$$

96 Here,  $u_i = (u, v, w)$  refers to the velocity along the  $x_i = (x, y, z)$  axes, corresponding to the  
 97 stream-wise (parallel to the bed), span-wise, and perpendicular (to the bed) directions,  
 98 respectively. The  $z = 0$  plane corresponds to the smooth bed. The overbar  $\bar{\phantom{x}}$  indicates a  
 99 time average, and a single prime  $'$  indicates deviation from the time average. The bracket  
 100  $\langle \phantom{x} \rangle$  indicates the spatial average. Each time-averaged variable  $\beta$  is expressed as the sum of  
 101 the spatial average,  $\langle \beta \rangle$ , and a deviation from the spatial average  $\beta''$ .  $p$  is the pressure,  
 102 and  $D_i$  is the mean vegetative drag in the  $i$  direction.  $\tau_{ij}^{disp}, \tau_{ij}^{Rey}, \tau_{ij}^{vis}$  are the dispersive

103 stress, local Reynolds stress and local viscous stress, respectively, defined in Eq.3.

$$104 \quad \tau_{ij}^{disp} = -\rho \langle \overline{u_i'' u_j''} \rangle \quad \tau_{ij}^{Rey} = -\rho \overline{u_i' u_j'} \quad \tau_{ij}^{vis} = \rho \nu \frac{\partial \overline{u_i}}{\partial x_j} \quad (3)$$

105 Here  $\nu$  is the kinematic viscosity. For gradually varying, unidirectional flow in a straight  
 106 channel,  $\left( \langle \overline{u} \rangle \frac{\partial \langle \overline{u} \rangle}{\partial x} \right) / \left( \frac{1}{\rho} \frac{\partial \langle \overline{p} \rangle}{\partial x} \right) \approx \frac{U^2}{gH}$ , with  $U$  representing the time and cross-sectional  
 107 averaged velocity. In our experiments,  $\frac{U^2}{gH} < 5\%$ , so that we neglect the non-uniformity  
 108 term in the  $x$ -momentum equation. Assuming that the average bed-normal ( $\langle \overline{w} \rangle$ ) and  
 109 lateral ( $\langle \overline{v} \rangle$ ) velocity are much smaller than the stream-wise velocity ( $\langle \overline{u} \rangle$ ), and that the  
 110 flow is steady ( $\frac{\partial \langle \overline{u_i} \rangle}{\partial t} = 0$ ), the stream-wise momentum equation can be simplified to Eq.4.

$$111 \quad 0 = g s_b - \frac{1}{\rho} \frac{\partial \langle \overline{p} \rangle}{\partial x} + \frac{1}{\rho} \frac{\partial}{\partial z} \left( \tau_{ij}^{disp} + \langle \tau_{ij}^{Rey} \rangle + \langle \tau_{ij}^{vis} \rangle \right) - D_x \quad (4)$$

112 Here  $s_b$  is the bed slope with respect to a horizontal plane. The vegetative drag  $D_x$  can  
 113 be represented by a quadratic law [e.g., Nepf, 2012a]:

$$114 \quad D_x = \frac{1}{2} \frac{C_D a}{(1 - \phi)} \langle \overline{u} \rangle^2 \quad (5)$$

115 Here  $a$  is the frontal area per canopy unit volume,  $\phi$  is the solid volume fraction, and  $C_D$   
 116 is the drag coefficient. For cylindrical stems,  $\phi = (\pi/4)ad$ . Assuming hydrostatic pressure  
 117 and small bed slope, the pressure gradient can be approximated as  $\frac{\partial \langle \overline{p} \rangle}{\partial x} = -\rho g (s_s - s_b)$ ,  
 118 where  $s_s$  is the water surface slope with respect to a horizontal plane. The fluid shear  
 119 stresses ( $\tau_{ij}^{disp}, \tau_{ij}^{Rey}, \tau_{ij}^{vis}$ ) go to zero at the water surface ( $z = Z_s$ ), so that a vertical  
 120 integration of Eq. 4 from water surface  $Z_s$  to any position  $z < Z_s$  yields,

$$121 \quad \left( \tau_{ij}^{disp} + \langle \tau_{ij}^{Rey} \rangle + \langle \tau_{ij}^{vis} \rangle \right) |_z + \rho \int_z^{Z_s} \left[ \frac{1}{2} \frac{C_D a}{1 - \phi} \langle \overline{u} \rangle^2 \right] dz = \rho g s (Z_s - z) \quad (6)$$

122 Here the potential gradient  $s$  is equal to the surface slope  $s_s$ . The left-hand side of Eq. 6  
 123 shows the partitioning of total flow resistance into the fluid shear stresses (first term) and



124 the vegetation drag (second term). The right-hand side of Eq.6 represents the driving  
 125 force for the flow due to potential gradient. A similar drag partition is described in  
 126 [Raupach and Shaw, 1982]. The no-slip condition at a smooth impermeable bed requires  
 127  $\tau_{xz}^{Rey}|_{z=0} = \tau_{xz}^{disp}|_{z=0} = 0$ , so that the spatially-averaged bed shear stress is simply  $\langle \tau_b \rangle =$   
 128  $\left( \tau_{ij}^{disp} + \langle \tau_{ij}^{Rey} \rangle + \langle \tau_{ij}^{vis} \rangle \right) |_{z=0} = \langle \tau_{xz}^{vis} \rangle |_{z=0} = \langle \rho \nu \frac{\partial \bar{u}}{\partial z} |_{z=0} \rangle$ . The effective friction velocity in  
 129 a heterogeneous flow field can be defined as:  $U_{*eff} = \sqrt{\langle \tau_b \rangle / \rho} = \sqrt{\langle \rho U_*^2 \rangle / \rho} = \sqrt{\langle U_*^2 \rangle}$ ,  
 130 with  $\tau_b$  and  $U_*$  defined as the local bed shear stress and local friction velocity, respectively.  
 131 In a homogeneous flow field, i.e. without vegetation,  $\tau_b = \langle \tau_b \rangle$  and  $U_* = U_{*eff} = \langle U_* \rangle$ .

## 2.2. Friction velocity over smooth beds

132 First, we consider flow over a smooth bed without vegetation, i.e. a bare channel, for  
 133 which the second term in Eq.6 is absent. In addition, for a bare channel the spatial  
 134 heterogeneity is small, and therefore the dispersive stress is negligible. Finally, for small  
 135  $s_s$  and  $s_b$ ,  $Z_s$  is approximately equal to the water depth,  $H$ , such that Eq. 6 can be  
 136 simplified to  $(\tau_{xz}^{Rey} + \tau_{xz}^{vis})|_z = \rho g s (H - z)$ , which indicates that the total stress, the sum  
 137 of the Reynolds stress and viscous stress, decreases linearly with distance from the bed  
 138 ( $z$ ). The same equation is given for bare channels by Nezu and Nakagawa [1993]. Note  
 139 that the local quantities and spatially-averaged quantities are the same in a bare channel.  
 140 As the Reynolds stress is zero at the bed,  $\tau_b = \rho U_*^2 = \tau_{xz}^{vis}|_{z=0} = \rho g s H$ , so that the bed  
 141 shear stress can be estimated from the potential gradient  $s = s_s$ , which for uniform flow is  
 142 also the bed slope ( $s_b$ ). Alternatively,  $U_*$  can be estimated by fitting the measured total  
 143 stress to the theoretical linear distribution of total stress,

$$144 \quad \tau_{tot}(z) = (\tau_{xz}^{Rey} + \tau_{xz}^{vis})|_z = \rho U_*^2 (1 - z/H) \quad (7)$$

145 In this paper, the application of Eq.7 will be called the total stress method.

146 Another common way to estimate the bed shear stress over a smooth bare channel is  
 147 to fit the measured velocity to the analytical velocity profile called the Law of the Wall  
 148 [*Kundu and Cohen, 2008; Nezu and Nakagawa, 1993*]:

$$149 \quad \frac{\bar{u}(z)}{U_*} = \begin{cases} \frac{zU_*}{\nu} = Z_+ & Z_+ \leq 5 \\ \frac{1}{\kappa} \ln\left(\frac{zU_*}{\nu}\right) + 5 & Z_+ \geq 30 \end{cases} \quad (8)$$

150 Here  $\kappa$ , the von Karman constant, is 0.41. This law is linear in the near-bed region  
 151 ( $Z_+ \leq 5$ ) and logarithmic above ( $Z_+ \geq 30$ ). A buffer layer exists between these two  
 152 regions, i.e.  $5 \leq Z_+ \leq 30$ , which is not described by the Law of the Wall.

153 Within a thin inner layer ( $Z_+ \leq 5$ ), the Law of the Wall assumes that the viscous stress  
 154 is constant, which is associated with a linear velocity profile (first line of Eq.8). In contrast  
 155 to this, if we assume that the Reynolds stress is negligible close to the bed, Eq.7 reduces  
 156 to  $(\tau_{xz}^{vis})|_z = \rho g s(H - z)$ , indicating that the viscous stress varies linearly with  $z$  close to  
 157 the bed, resulting in a near-bed velocity profile that is parabolic. We define the height  
 158 of the region dominated by viscous stress,  $H_v$ , as the height above the bed at which the  
 159 linear distribution of viscous stress reaches zero, which corresponds to the height above  
 160 the bed at which the parabolic portion of the velocity profile ends. Very close to the wall  
 161 ( $Z \ll H_v$ ), the linear velocity distribution proposed in the Law of the Wall is a good  
 162 approximation to the parabolic velocity distribution.

163 The linear viscous stress distribution and the associated parabolic velocity profile can  
 164 be expressed as:

$$165 \quad \tau^{vis} = \rho \nu \frac{\partial \bar{u}}{\partial z} = \rho \frac{U_*^2}{H_v} (H_v - z) \quad z \leq H_v \quad (9)$$

$$166 \quad \bar{u}(z) = \frac{U_*^2}{\nu} \left( z - \frac{z^2}{2H_v} \right) \quad z \leq H_v \quad (10)$$

168 Note that because the flow is homogeneous in a bare channel, the locally-defined equations  
 169 (Eq.7, 8, 9 and 10) are also valid for spatially-averaged values, i.e. also apply if the local  
 170 velocity  $\bar{u}$  and the local friction velocity  $U_*$  are replaced by the spatially -averaged velocity  
 171  $\langle \bar{u} \rangle$  and the spatially-averaged friction velocity  $\langle U_* \rangle$ .

172 Now we consider the situation with vegetation on a smooth bed. However, we specif-  
 173 ically consider regions of the flow for which the distance to the bed is smaller than the  
 174 distance to the nearest stem, such that the viscous stress and the velocity are controlled  
 175 by the proximity to the bed in a manner similar to that described above for the bare chan-  
 176 nel. Namely, the near-bed viscous stress should also follow the linear-stress model. We  
 177 anticipate that this description will fail at some distance close to a cylinder, at which the  
 178 cylinder surface also contributes to local viscous stress. In addition, we specifically note  
 179 that this description will not hold within one diameter of each cylinder (stem), because  
 180 of secondary flow structures that exist in this region (e.g. [Stoesser *et al.*, 2010]). In a  
 181 model canopy of emergent vegetation with uniform frontal area (array of circular cylin-  
 182 ders), previous studies [Nepf, 1999; Nikora *et al.*, 2004; Liu *et al.*, 2008] have shown that  
 183 the stream-wise velocity in the upper water column (i.e. away from the bed) is vertically  
 184 uniform, such that  $\tau^{vis} = \rho\nu \frac{\partial \bar{u}}{\partial z} = 0$ . We therefore propose the following model for the  
 185 distribution of viscous stress in regions at least one diameter away from the stems inside  
 186 an emergent canopy:

$$187 \quad \tau^{vis} = \begin{cases} \rho \frac{U_*^2}{H_v} (H_v - z) & z < H_v \\ 0 & z \geq H_v \end{cases} \quad (11)$$

188 The following velocity distribution is consistent with (11) and a no-slip condition at the  
 189 bed:

$$190 \quad \bar{u}(z) = \begin{cases} \frac{U_*^2}{\nu} \left( z - \frac{z^2}{2H_v} \right) & z \leq H_v \\ \frac{U_*^2 H_v}{2\nu} & z \geq H_v \end{cases} \quad (12)$$

191 Denoting the local time-averaged stream-wise velocity in the uniform layer ( $z \geq H_v$ ) as  
 192  $U_o$ , the local friction velocity  $U_*$  can be calculated from Eq. 12.

$$193 \quad U_* = \sqrt{\frac{2\nu U_o}{H_v}} \quad (13)$$

194 In this study, we use laboratory measurement to examine the validity of Eq.13 and to  
 195 look for connections between  $H_v$  and the characteristics of the model canopy. In addition,  
 196 we evaluate the relationship between the local estimate of  $U_*$ , denoted in Eq.13, and the  
 197 effective friction velocity ( $U_{*eff} = \sqrt{\langle U_*^2 \rangle}$ ) associated with the spatially-averaged bed  
 198 shear stress.

### 3. Methods

199 Laboratory experiments were conducted in a horizontal recirculating glass flume with  
 200 a 1.2m-wide and 13m-long test section (bed slope  $s_b = 0$ ). By varying the weir height at  
 201 the end of the flume, the water depth was varied between  $H = 0.07m$  and  $H = 0.13m$ . By  
 202 varying the pump frequency, the cross-sectional average velocity was varied between 0.002  
 203 and 0.18 m/s. A backscatter Laser Doppler velocimetry (LDV) probe (Dantec Dynamics)  
 204 was mounted on a manually driven positioning system. Simultaneous measurements of  
 205 stream-wise ( $u$ ) and vertical ( $w$ ) velocity were recorded over a 300s period. The positioning  
 206 system allowed the LDV to move in both the  $z$  and  $y$  directions with a resolution of  
 207 0.1mm. In order to measure velocity very close to the bed, the LDV axis was tilted 1  
 208 deg from horizontal and the velocity was later corrected for this tilt. The wavelengths

209 of the two beams of the LDV were 514.5 and 488nm, and the focal length was 399mm.  
210 For the majority of positions the sampling frequency was 125Hz, but close to the bed  
211 the sampling frequency dropped as low as 5Hz. At this frequency, the mean velocity was  
212 still reliably measured, but not the Reynolds stress. In these cases the near bed Reynolds  
213 stress measurements were excluded from further analyses, as noted below. The sampling  
214 volume was  $4mm \times 0.2mm \times 0.2mm$  in the  $y$ ,  $x$ , and  $z$  direction, respectively. The flow  
215 was seeded with pliolite particles, and because the PVC board on the bottom of the flume  
216 was black, the reflection from the bed was negligible.

217 To simulate emergent vegetation, rigid dowels were placed in a staggered array with  
218 spacing  $ds$ . The array was held in place by perforated, black, PVC baseboards with  
219 smooth surfaces as shown in Fig.1. The dowels covered the full width of the flume. Two  
220 cylinder sizes were considered, with diameter  $d = 0.0063m$  and  $d = 0.0126m$ . The frontal  
221 area per unit volume ranged from  $a = 0.5m^{-1}$  to  $17.8m^{-1}$ . The drag coefficient for the  
222 cylinders in the array,  $C_D$ , was estimated from a previous study [Tanino and Nepf, 2008].  
223 20 trials with dowels and 4 with a bare channel were conducted (Table 1). For each trial,  
224 the velocity was measured at 15 to 40 positions along 3 to 11 vertical profiles, with at least  
225 4 profiles for a vegetated channel. Our experiments have shown that in a canopy 4 profiles  
226 give a good estimation of the laterally-averaged parameters if the profiles are recorded  
227 at the extrema of the velocity field (i.e one profile just behind a dowel  $y/ds = 0$ , one  
228 profile behind the closer adjacent dowel in the upstream row  $y/ds = 1$ , one profile at the  
229 maximum velocity between the two previous dowels  $y/ds = 0.5$ , and one profile between  
230 the maximum velocity and the minimum velocity  $y/ds = 0.25$ ). The vertical spacing  
231 of measurements was 0.2mm near the bed. For the denser canopies ( $a = 12.6m^{-1}$  and

232  $17.3m^{-1}$ ), 2 or 3 dowels at the side of the flume were removed to clear the optical path.  
 233 Because the cylinders were removed from positions laterally adjacent to the measurement  
 234 point, their removal did not alter the flow development leading up to the measurement  
 235 point. Details about each trial can be found in Table 1. Due to the constraint of optical  
 236 access, the individual vertical profiles were positioned along a lateral transect mid-way  
 237 between rows. The transect is shown in Fig.1b. In this paper, a spatial-average ( $\langle \rangle$ )  
 238 denotes the lateral-average along this particular transect. The friction velocity estimated  
 239 from the spatially-averaged velocity is denoted  $\langle U \rangle_*$ , and the spatial-average of the local  
 240 estimates of friction velocity  $U_*$ , i.e. based on individual velocity profiles, is denoted  $\langle U_* \rangle$ .  
 241 The relationship among  $\langle U \rangle_*$ ,  $\langle U_* \rangle$  and  $U_{*eff}$  is discussed in section 4.1.2 and 5.1.

242 The measured velocities were used to estimate the friction velocity by fitting the Law of  
 243 the Wall (Eq.8), and the new linear stress model (Eq.10 and 12 ). For the Law of the Wall,  
 244  $U_*$  was used as the fitting parameter, and the best fit was chosen based on the minimum  
 245 value of the sum-of-squares error (SSE) between the measurements and the model for  
 246 both  $Z_+ \leq 5$  and  $Z_+ \geq 30$  region, i.e. the two regions were fitted together in a single  
 247 procedure. The uncertainty in the fit was evaluated by finding the range of  $U_*$  values that  
 248 return SSE less than the standard deviation amongst the individual measured profiles.  
 249 For the new linear stress model, both  $U_*$  and  $H_v$  were used as fitting parameters for Eq.12  
 250 with the best combination of values returning the lowest SSE. The uncertainty of  $U_*$  and  
 251  $H_v$  were tuned separately using the same method as the Law of the Wall. Assuming that  
 252 the spatially-averaged velocity profile follows the two-layer velocity distribution described  
 253 by Eq.12, we can also fit  $\langle \bar{u} \rangle$  to define an associated  $\langle U \rangle_*$  and  $H_{vo}$ . The measurements  
 254 described later in the paper will support this assumption. Correspondingly,  $\langle U \rangle_*$  and

255  $H_{v0}$  were estimated by fitting Eq.12 to the spatially-averaged velocity profile following  
 256 the same procedure. Finally, for the bare channel cases, the friction velocity was also  
 257 estimated by fitting Eq.7 over  $Z_+ \geq 30$ , which we call the total stress method.  $U_*$  was  
 258 chosen based on the minimum SSE between  $\rho U_*^2(1 - z/H)$  and  $(\tau_{xz}^{Rey} + \tau_{xz}^{vis})|_z$  with the  
 259 stresses estimated from measured velocity data (Eq.3). At  $Z_+ \leq 30$ ,  $(\tau_{xz}^{Rey} + \tau_{xz}^{vis})|_z$ ,  
 260 oscillates intensely with the adjacent value differing by up to 20%. We therefore exclude  
 261 data from  $Z_+ \leq 30$  from the fit. The uncertainty of  $U_*$  was then determined from the  
 262 range of  $U_*$  that return a SSE less than the spatial variation between individual local total  
 263 stress  $((\tau_{xz}^{Rey} + \tau_{xz}^{vis})|_z)$  profiles. For convenience, the spatially-averaged value were used  
 264 in all the fittings for bare channel cases, because of the homogeneity of the flow.

## 4. Results

### 4.1. Linear distribution of near-bed viscous stress

#### 4.1.1. Flow over a smooth bare channel

265 We first consider the smooth bare channel. The vertical distribution of normalized  
 266 spatially-averaged stresses and stream-wise velocity are shown in Fig. 2 for case 1.1.  
 267 The  $U_*$  obtained from the total stress method is used in the normalization. Near the  
 268 bed ( $z_+ \leq H_{v+}$ ), the viscous stress (triangles) had a linear distribution, supporting the  
 269 linear stress model described above. For  $z_+ = zU_*/\nu \leq 5$  the Law of the Wall and the  
 270 linear stress model did equally well in describing the measured velocity (compare the gray  
 271 dashed curve and the black dot-dash curve in Fig.2b). However, unlike the Law of the  
 272 Wall, the linear stress model also represented the measured velocity for  $z_+ \geq 5$ , up to  
 273  $z_+ \approx 25$ . That is, the new linear stress model provides a description of the velocity profile  
 274 that extends through the buffer layer ( $5 < Z_+ < 30$ ).

276 For the bare channel conditions, three methods were used to estimate the bed shear  
 277 stress: the Law of the Wall (Eq. 8), the total stress method (Eq.7), and the new linear  
 278 stress model (Eq. 10). The bed shear stress estimated from the Law of the Wall and  
 279 the linear stress method agreed within uncertainty (Table 2) for cases 1, 2 and 3, and  
 280 differed by only 14% for case 4. This agreement makes sense, because near the wall  
 281 ( $Z_+ < 5$ ), the velocity profiles associated with each fit essentially overlap (Fig. 2b). The  
 282 total-stress method also produced values of  $U_*$  in agreement (within uncertainty) with the  
 283 two velocity laws, providing a consistency check for the estimated  $U_*$ . Finally, the non-  
 284 dimensional linear-stress layer height,  $H_{v+} = H_v U_* / \nu$  (using  $U_*$  from the new linear stress  
 285 model), had a consistent value across all four cases (within uncertainty), suggesting that  
 286  $H_{v+} = 22 \pm 3(SD)$  may be a universal constant, although further verification is required.  
 287 Like the viscous sublayer thickness defined in the Law of the Wall ( $Z_+ = 5$ ),  $H_v$ , defines  
 288 a region near the bed dominated by viscous stress, so it is not surprising that it may also  
 289 have a universal value.

#### 290 4.1.2. Flow over smooth channels with emergent vegetation

291 Compared with the bare channel cases, the distribution of stresses within the emergent  
 292 canopy was more complicated because two additional components were added by the  
 293 canopy: the dispersive stress and the vegetative drag (Fig. 3a). The vegetative drag,  
 294 estimated by Eq. 5, represented 97% of the potential forcing and dominated the flow  
 295 resistance over the entire water column. Because the total stress was dominated by  
 296 vegetation drag, the total stress normalized by the bed shear stress,  $\rho \langle U \rangle_*^2$ , was much  
 297 larger than 1 at the bed. The vertical profiles of viscous stress at eleven positions within  
 298 the array are shown in Fig. 3b. Although the velocity varied spatially inside the canopy



(Fig. 4 and 5a), the viscous stress had almost no variation along the measurement transect. This gives support to the assumption made above that our transect represents a region of the flow for which the viscous stress distribution is dominated by the proximity to the bed, because the distance to the bed is smaller than the distance to the nearest stem. Further, the viscous stress was linear near the bed and zero in the upper layer (Fig.3b), which agreed with the linear stress model given in Eq.11. The dispersive stress and the Reynolds stress, though comparable to the viscous stress near the bed, reduce to zero at the bed, so the bed shear stress equals the viscous stress at the bed, i.e. the normalized viscous stress goes to 1 (Fig. 3c).

The individual vertical profiles of time-averaged, stream-wise velocity normalized by  $\langle U \rangle_*$  at 11 lateral positions are shown in Fig. 4. Here  $\langle U \rangle_*$  was derived from the fit of the linear-stress model (Eq.12) to the spatially-averaged velocity profile. At each lateral position, the velocity profiles were consistent with the two-zone profile proposed in Eq. 12. Specifically, the velocity was vertically uniform in the upper canopy ( $z/d \geq 4$ ), and the velocity near the bed ( $z/d < 0.5$ ) was parabolic (gray dot-dash curves in Fig. 4b).

The spatially and time averaged velocity (the black curve in Fig. 5) also supported the linear stress model, i.e. the spatially-averaged velocity was vertically uniform in the upper canopy ( $z/d \geq 4$ ) and parabolic in the near-bed region ( $z/d \leq (H_{vo})/d$ ). Here  $H_{vo}$  was derived from the fit of the linear-stress model (Equation 11) to the spatially-averaged velocity profile, the same as  $\langle U \rangle_*$ . Note again how the parabolic velocity profile provided a good fit to the spatially-averaged velocity over a larger distance (up to  $Z_+ = H_{vo} \langle U \rangle_* / \nu = 19$ ) than the Law of the Wall, which is only valid up to  $Z_+ = 5$ . However, similar to measurements described in *Liu et al.* [2008] a region of velocity deviation was

322 observed close to  $Z_+ = H_{vo+}$ . The Reynolds stress exhibited a local maximum at the same  
 323 distance above the bed (circles, Fig. 3c). The feature deteriorates with increasing lateral  
 324 distance from the upstream cylinder (Fig.4) suggesting it is associated with the horseshoe  
 325 or junction vortex formed at the bed near each cylinder base (see Fig.7 in [Stoesser *et al.*,  
 326 2010]). These coherent structures scale with the cylinder diameter.

327 We next consider the relationship between  $\langle U \rangle_*$  and  $H_{vo}$ , fitted from the spatially-  
 328 averaged velocity, and the locally fitted  $U_*$  and  $H_v$  (Fig.6). Along the lateral transect  
 329 (defined in Fig.1), the local friction velocity  $U_*(y)$  was fairly uniform, varying by a max-  
 330 imum of 30% from  $\langle U \rangle_*$ . The minimum  $U_*(y)$  occurred directly behind the upstream  
 331 dowel ( $y = 0$ ), which was reasonable because the velocity was also minimum here. The  
 332 spatial-average of the local  $U_*$ , denoted as  $\langle U_* \rangle$ , was approximately equal to  $\langle U \rangle_*$  (within  
 333 10% uncertainty). To conclude, Fig.4, 5 and 6 taken together have shown that along the  
 334 measurement transect, the new linear stress model (Eq.11) fits both the local velocity pro-  
 335 files and the spatially-averaged profile. In addition, despite the variation in upper-water  
 336 column velocity ( $U_o$ ) across the transect (Fig.5), the friction velocity was fairly constant,  
 337 such that either order of averaging and fitting ( $\langle U \rangle_*$  versus  $\langle U_* \rangle$ ) produced similar values.  
 338 In the following sections we focus on developing an estimator for  $\langle U \rangle_*$ . More discussions  
 339 on how  $\langle U \rangle_*$  or  $\langle U_* \rangle$  can be used to estimate the effective friction velocity at the canopy  
 340 scale is presented in section 5.1.

## 4.2. The scale of $H_{vo}$

### 4.2.1. The scale of $H_{vo}$ at low $Re_H$ for $a \geq 4.3m^{-1}$

342 The values of  $H_{vo}$  determined from the linear stress model fit to the spatially-averaged  
 343 velocity are plotted in Fig.7. Subplot (a) and (b) separate the cases by cylinder diameter,

344  $d = 6.3$  and  $12.6\text{mm}$ , respectively. First, we consider the smaller cylinder size (Fig.7a).  
 345 When the array had sufficient density ( $a = 4.3\text{m}^{-1}$  and  $17.3\text{m}^{-1}$ , shown with squares and  
 346 up triangles),  $H_{vo}$  was comparable to the stem radius (shown by horizontal dashed line).  
 347 If the depth Reynolds number was not too high ( $Re_H \leq 6000$ ), at similar values of  $Re_H$ ,  
 348  $H_{vo}$  in the sparse canopy (gray circles) and the bare channel (open circles) were clearly  
 349 larger than the stem radius. Therefore the presence of a dense canopy ( $a \geq 4.3\text{m}^{-1}$ )  
 350 reduced the linear-stress layer thickness to a scale comparable to  $d/2$  for small depth  
 351 Reynolds number (e.g.  $Re_H < 6000$ ). For simplicity,  $R = d/2$  is used in the following  
 352 paragraphs. However, in sparse canopies ( $a = 0.5\text{m}^{-1}$  in Fig.7a, gray circles),  $H_{vo}$  was  
 353 larger than the stem radius  $R$ . Specifically, the sparse canopy value of  $H_{vo}$  was between  
 354 the bare channel value and the value in a dense canopy ( $R$ ). We propose that at low depth  
 355 Reynolds number (e.g.  $Re_H < 6000$ ), for canopies of sufficient density (here  $a \geq 4.3\text{m}^{-1}$ ),  
 356 the viscous sub-layer is restricted to the scale of the cylinder radius. The relationship  
 357 between  $H_{vo}$  and  $R$  observed for dense canopies ( $a \geq 4.3\text{m}^{-1}$ ) is likely associated with  
 358 the coherent structures formed near the base of each stem. These structures create strong  
 359 vertical velocity near the bed, as shown by *Stoesser et al.* [2010]. In particular, Fig.5 in  
 360 *Stoesser et al.* [2010] shows strong vertical velocity occurs near  $z = R$ . By enhancing  
 361 vertical momentum transport near the bed, the coherent structures may suppress  $H_{vo}$  to  
 362 a scale comparable to  $R$ .

#### 363 4.2.2. Dependence on $Re_H$

364 As  $Re_H$  increased, the bare channel values of  $H_{vo}$  decreased (Fig.7a), which is consistent  
 365 with the constant value observed for  $H_{vo+} = (H_{vo} \langle U \rangle_*) / \nu = 22 \pm 3$  (Table 2). As  $\langle U_o \rangle$   
 366 increases,  $\langle U \rangle_*$  also increases, so that  $H_{vo}$  decreases. The same trend was observed for the

367 viscous sub-layer defined by the Law of the Wall ( $\delta_s$ ), i.e.  $\delta_{s+} = 5$ , so that as  $\langle U_o \rangle$  increases,  
 368  $\delta_s$  decreases. In our study,  $H_{vo}$  in the bare channel became comparable to the smaller  
 369 stem radius ( $d = 6.3mm$ ) near  $Re_H = 8000$  (Fig.7a), so that above this value of  $Re_H$ ,  
 370 the presence of the canopy had little impact on the value of  $H_{vo}$ . Although not evident  
 371 in the cases we tested, we conjecture that if  $Re_H$  was increased further ( $Re_H > 8000$ ),  
 372 the bare channel  $H_{vo}$  would become smaller than  $R$ . Accordingly, we posit that there  
 373 exists a Reynolds number above which the linear-stress layer thickness,  $H_{vo}$ , would be the  
 374 same in both bare and vegetated channels, because the constraint imposed on  $H_{vo}$  by bed-  
 375 generated turbulence would be greater than the constraint imposed by the stem-generated  
 376 turbulence.

377 Now we consider the larger size cylinders ( $d = 12.6mm$ , Fig.7b). The values of  $H_{vo}$   
 378 observed with the larger diameter arrays were consistent with conclusions drawn above  
 379 based on the smaller diameter arrays. Because the size constraint imposed by the stem  
 380 radius was larger ( $R = 6.3mm$ ), the bare channel value of  $H_{vo}$  became comparable to  $R$   
 381 at a lower  $Re_H$  than occurred with the smaller radius arrays ( $R \approx 3.2mm$ ). Specifically,  
 382 the bare and vegetated channel values of  $H_{vo}$  became comparable to one another within  
 383 uncertainty at  $Re_H = 4000$ . At higher  $Re_H$ , there was no difference between the bare  
 384 channel and emergent array conditions. To summarize, below a transition  $Re_H$ , a dense  
 385 canopy ( $a \geq 4.3m^{-1}$ ) can suppress  $H_{vo}$  to  $R$ , but at higher  $Re_H$ ,  $H_{vo}$  is the same in  
 386 both bare and vegetated channels. The transition  $Re_H$  decreases with increasing stem  
 387 radius. Based on this, we suggest that the linear-stress layer thickness in a dense canopy  
 388 ( $a \geq 4.3m^{-1}$ ) will be  $H_{vo} = \min(R, 22\nu/\langle U \rangle_*)$ , where the later term denotes the value  
 389 for a bare bed.

390 The fitted  $H_{vo}$  normalized by  $\min(R, 22\nu/\langle U \rangle_*)$  are shown in Fig.8. For the bare  
 391 channel and emergent channels with  $a \geq 4.3m^{-1}$ , the model gives a very robust prediction  
 392 of  $H_{vo}$ , with these cases falling along the line of model agreement, shown by the horizontal  
 393 dashed line. The proposed model for  $H_{vo}$  fails for sparse arrays ( $a = 0.5m^{-1}$ , gray circles).

### 4.3. Estimation of $\langle U \rangle_*$ in an emergent canopy

394 As shown in Fig.5, the spatially-averaged velocity can also be fit to Eq.13, producing  
 395 the estimate  $\langle U \rangle_* = \sqrt{\frac{2\nu\langle U_o \rangle}{H_{vo}}}$ . Below the transition  $Re_H$ , which varies with stem radius  
 396 and bed texture, we propose that the friction velocity  $\langle U \rangle_* = 2\sqrt{\frac{\nu\langle U_o \rangle}{d}}$ . As discussed  
 397 above, this scaling fails if the canopy is too sparse, such that the stem-scale coherent  
 398 structures do not dominate the near-bed flow, or if the depth Reynolds number is too  
 399 high, such that the bed-driven turbulence places a stronger constraint on  $H_{vo}$  than the  
 400 stem related turbulence. To reflect the influence of both bed-driven and stem-driven  
 401 near-bed turbulence, we propose the following relationship for dense emergent canopies:

$$402 \quad \langle U \rangle_* = \max \left( \sqrt{C_f} \langle U_o \rangle, 2\sqrt{\frac{\nu \langle U_o \rangle}{d}} \right) \quad (14)$$

403 Here,  $C_f$  denotes the drag coefficient for the bare bed, and is a function of bed texture.  
 404 Note that although  $\langle U_o \rangle$  strictly defines the spatial-average of the velocity in the uniform  
 405 upper layer of the canopy, in most cases  $\langle U_o \rangle$  is close to the cross-sectionally averaged  
 406 velocity, which is denoted as  $U$  in Table 1, which is also the volume flow rate per unit  
 407 cross-sectional area corrected for porosity. Eq.14 captures the physical limit that at high  
 408 Reynolds number the vegetation will have negligible influence on  $H_{vo}$  and  $\langle U \rangle_*$ . This limit  
 409 is demonstrated in the values of  $\langle U \rangle_*$  shown in Fig. 9a. For the two stem diameters we  
 410 studied, when  $Re_H$  was higher than 8000, the non-dimensional friction velocity  $\langle U \rangle_* / \langle U_o \rangle$

411 in the emergent canopy was close to the value observed in the bare channel, regardless of  
 412 the stem diameter and the density of the canopy. However, at low and moderate  $Re_H$ ,  
 413  $\langle U \rangle_* / \langle U_o \rangle$  in dense canopies (squares, triangles, and pentagrams) was higher than bare  
 414 channel values in Fig. 9a. Note that the transition  $Re_H$  should decrease as  $d$  increases.  
 415 That is, for a larger stem diameter, the bare channel value of  $H_{vo}$  would reach  $R$  at a  
 416 lower  $Re_H$ . We caution that the transition  $Re_H$  will likely also depend on the bare bed  
 417 texture which influences  $C_f$ . The quantification of  $C_f$ , however, was not the focus of this  
 418 study. Here we assume that  $C_f$  for the bare channel is already known, and concentrate  
 419 on quantifying the bed shear stress once cylinder arrays have been added to the bare bed.

420 Finally, Fig. 9b depicts  $\langle U \rangle_*$  non-dimensionalized by  $\sqrt{(\nu \langle U_o \rangle) / d}$  for  $Re_H \leq 6000$ .  
 421 Over this range of  $Re_H$ ,  $\langle U \rangle_* / \langle U_o \rangle$  was enhanced by dense canopies with stem diameter  
 422  $d = 6.3mm$  (the squares and up triangles in Fig. 9a). Compared with the scatter of  
 423  $\langle U \rangle_* / \langle U_o \rangle$  over the same range of  $Re_H$  shown in Fig. 9a, the  $\langle U \rangle_*$  non-dimensionalized  
 424 by  $\sqrt{(\nu \langle U_o \rangle) / d}$  was roughly a constant ( $\approx 2$ ) as shown in Fig. 9b. This observation con-  
 425 firmed that for this range of conditions  $\langle U \rangle_*$  might be estimated as  $\langle U \rangle_* \approx 2\sqrt{(\nu \langle U_o \rangle) / d}$ .  
 426 In order to test the robustness of the conceptual model, the  $\langle U \rangle_*$  obtained from Eq.14  
 427 normalized by  $\langle U_o \rangle$  was plotted against the fitted  $\langle U \rangle_*$  normalized by  $\langle U_o \rangle$  in Fig.10. As  
 428 shown in the figure,  $\langle U \rangle_* / \langle U_o \rangle$  for the bare bed cases (open circles) collapse to a single  
 429 point, indicating that  $\langle U \rangle_* / \langle U_o \rangle$  is a constant for bare bed channels with the same bed  
 430 texture. In the channels with model vegetation, however,  $\langle U \rangle_* / \langle U_o \rangle$  has a wide range of  
 431 values. The proposed model (Eq.14 and the dashed line in Fig.10) captures the variation  
 432 of  $\langle U \rangle_* / \langle U_o \rangle$  in an emergent canopy with density  $a \geq 4.3m^{-1}$ . For  $a = 0.5m^{-1}$ , however,

433 the model over-predicts  $\langle U \rangle_* / \langle U_o \rangle$ . More extensive testing is needed to more precisely  
 434 define the array density above which Eq.14 applies.

## 5. Discussion

### 5.1. Relationship between the measurement transect and the canopy average

435 As discussed in section 4.1.2, the friction velocity  $\langle U \rangle_*$ , fitted from the spatially-averaged  
 436 velocity  $\langle U \rangle$  along the measurement transect (Fig. 1), falls within 10% of  $\langle U_* \rangle$ , the spatial-  
 437 average of the local  $U_*$  (Fig.6). In this section, we use the numerically simulated data from  
 438 *Salvador et al.* [2007] to show that  $\langle U_* \rangle$  may be a good approximation for the effective  
 439 friction velocity  $U_{*eff}$  ( $= \sqrt{\langle U_*^2 \rangle}$ ) within some uncertainty. The simulation results are  
 440 shown in Fig.11. We first exclude the data in the region within one diameter from the  
 441 center of each stem (Fig.11). We justify this exclusion based on the fact that we seek an  
 442 estimate of bed shear stress for the future purpose of predicting net sediment flux through  
 443 the canopy. The elevated (red) and diminished (blue) regions of bed stress close to the  
 444 individual cylinders only produce localized sediment transport, i.e. the scour holes and  
 445 deposition mounds classically observed near bridge piers (Fig.1 in [*Yager, 2013*]), and are  
 446 not indicators of sediment flux at the canopy scale. Specifically, *Hongwu et al.* [2013]  
 447 observed that the generation of individual scour holes occurs at lower channel velocities  
 448 than the onset of canopy-scale sediment transport. Therefore, we suggest that the value of  
 449 bed shear stress within the contiguous region of relatively uniform bed shear stress (green  
 450 region in the color map) represents the more relevant value for predicting canopy-scale  
 451 sediment transport.

452 After excluding data from within 1 diameter of each stem center, we laterally-averaged  
 453 the local  $U_*$  at each  $x$  position (upper plot in Fig.11). This lateral-average of local  $U_*$  is

denoted as  $\langle U_* \rangle_L$ . The position  $x/ds = 1$  corresponds to the measurement transect used in this study, and this point is marked in Fig.11. The average of  $\langle U_* \rangle_L$  along the  $x$  direction, denoted as  $\langle U_* \rangle_A$ , is the canopy-scale area average of  $U_*$ . Fig.11 shows the variation  $\langle U_* \rangle_L$ , normalized by the shear velocity associated with the total stress  $\sqrt{gHs}$ , along  $x$  (blue curve). Note that since vegetative drag also contributes to the total stress, this normalized bed shear stress has an average value less than 1. In the region between cylinders, e.g.  $x/ds = 0.5$  to  $1.5$ ,  $\langle U_* \rangle_L$  is relatively uniform, and close to  $\langle U_* \rangle$  (marked in figure). Further,  $\langle U_* \rangle$  differs from  $\langle U_* \rangle_A$  (blue dashed line) by only 10%. For arrays with larger spacing between cylinders, the uniform region will occupy a larger fraction of the total area, and the difference between  $\langle U_* \rangle$  and  $\langle U_* \rangle_A$  will decrease. We therefore tentatively suggest that  $\langle U_* \rangle$  is representative of the canopy-average. In addition, the effective friction velocity, defined as  $U_{*eff} = \sqrt{\langle U_*^2 \rangle}$  (black dashed line Fig.11) is approximately equal to the  $\langle U_* \rangle_A$  (within 5%). Given this, we suggest that Eq.14 may reasonably predict the effective friction velocity  $U_{*eff}$ :

$$U_{*eff} = \max \left( \sqrt{C_f} \langle U_o \rangle, 2\sqrt{\frac{\nu \langle U_o \rangle}{d}} \right) \quad (15)$$

We caution that this conclusion is tentative, because *Salvador et al.* [2007] only provides maps of bed shear stress for a single case,  $Re_H \approx 3000$  and  $ds = 2.5d$ .

## 5.2. Limitations of the model

The linear-stress model developed in this study has several limitations. Firstly, it only works when the frontal area per unit canopy volume  $a$  is large enough so that the velocity in the upper water column is uniform and that the stem generated turbulence is strong



474 enough to limit the scale of  $H_v$  to  $R$ . In our experiments, we found that these conditions  
 475 are met for  $a \geq 4.3m^{-1}$ .

476 Secondly, the vegetation center-to-center spacing  $2ds$  (as shown in Fig.1) should be  
 477 larger than twice the stem diameter  $2d$ . As discussed in section 2.2, within one diameter  
 478 of the stem center, the local linear stress model does not hold because the horseshoe  
 479 vortex system generated at the stem base locally alters the stress distribution. In addition,  
 480 as the center-to-center spacing ( $2ds$ ) decreases below  $5d$ , the case shown in Fig.11, the  
 481 region where  $\langle U_* \rangle_L$  is uniform also decreases. As a result the difference between  $\langle U_* \rangle$  and  
 482  $U_{*eff}$  would increase, degrading the accuracy of the shear-stress estimate given in Eq.15.  
 483 However, for  $ds/d = 2.5$ , the difference between  $\langle U_* \rangle$  and  $U_{*eff}$  is only 15% (Fig.11),  
 484 implying that Eq.15 is accurate to within 15%.

485 Thirdly, the model and experiments described here only consider smooth and imper-  
 486 meable beds. Using the distinction between hydraulically rough and smooth flows as a  
 487 guide, we expect that the validity of the proposed model for rough beds would depend  
 488 on the relative size of the bed roughness (sediment size) and thickness of the linear-  
 489 stress layer. For example, in a salt marsh,  $\langle U_o \rangle$  may be between 1 and 10cm/s and  
 490 typical stem sizes are  $d = 0.1$  to 1cm, such that the thickness of the linear-stress layer  
 491  $H_{vo} = \min(R, 22\nu/\sqrt{C_f}\langle U_o \rangle)$  is on the order of 1mm, which is larger than the sediment  
 492 size (on the order of 0.1mm). In this case the model developed for smooth beds may  
 493 provide a reasonable estimate of  $U_*$ . In contrast, on a floodplain  $\langle U_o \rangle$  may be 1m/s or  
 494 higher and  $d$  is  $O(10cm)$ , so that  $H_{vo}$  is on the order of 0.1mm which is comparable to  
 495 sediment size. In this case, the bed roughness extends beyond what we expect to be  
 496 the linear-stress layer, and we expect that the bed roughness will alter near-bed dynam-

497 ics. Possibly this adjustment may be accomplished with an adjustment to  $C_f$  to reflect  
498 the appropriate roughness, but a firm conclusion cannot be drawn until experiments are  
499 completed on rough, permeable beds.

500 It is important to note that the spatial-averaging discussed in this paper (and especially  
501 section 5.1) was targeted only at bed shear stress. The relationships between local values  
502 and area-averages cannot be extended to other quantities, such as velocity or dispersive  
503 stress. In addition, the model here only considers emergent vegetation with cylindrical  
504 geometry. To apply the model for submerged vegetation, the frontal area index  $ah$  ( $h$  is  
505 the height of the vegetation) has to satisfy  $ah \geq 0.3$  so that the turbulence generated at  
506 the top of the submerged canopy does not penetrate to the bed and affect the near bed  
507 stress distribution ([*Luhar et al.*, 2008]). For vegetation with non-uniform frontal area,  
508  $a(z)$ , the velocity in the upper layer of the canopy will not be uniform, instead varying  
509 inversely with  $a$  in  $z$  direction [*Nikora et al.*, 2004]. In this case, the upper layer velocity  
510  $\langle U_o \rangle$  will need to be defined more carefully.

## 6. Conclusion

511 This study developed a model that can predict the friction velocity in smooth channels  
512 with and without model emergent vegetation. In a bare channel, the model assumes that  
513 within a distance  $H_v$  from the bed, the Reynolds stress is negligible so that the viscous  
514 stress decreases linearly with increasing distance from the bed. The experimental data  
515 confirm the near-bed linear distribution of viscous stress and suggest a universal value for  
516 the non-dimensional layer thickness  $H_{v+} = 22 \pm 3$ . Within a model canopy of emergent  
517 cylindrical dowels, the linear stress distribution was observed in regions more than one  
518 diameter from the center of each dowel (Fig.4). For canopy density above  $4.3m^{-1}$ , the

519 thickness of the linear stress layer ( $H_v$ ) was shown to be the minimum of the stem radius  
520 ( $d/2$ ) and the bare channel value ( $22\nu/\langle U \rangle_*$ ), such that the effective friction velocity can  
521 be estimate from  $U_{*eff} = \max\left(\sqrt{C_f}\langle U_o \rangle, 2\sqrt{\frac{\nu\langle U_o \rangle}{d}}\right)$ . The effective friction velocity in  
522 an emergent canopy is therefore either larger than or equal to the bare channel value, for  
523 comparable depth-average velocity.

524 **Acknowledgments.** The work was supported by NSF Grant EAR 1414499. The data  
525 for the color map in Fig.11 is provided by Guillermo Palau Salvador, Thorsten Stoesser,  
526 Andreas Christof Rummel, and Wolfgang Rodi. The velocity data used in the paper is  
527 available in excel format upon request from the authors. The data are archived at MIT  
528 Parsons Lab. We also thank Francesco Ballio and two other anonymous reviewers for  
529 their useful comments.

## References

- 530 Abbe, T. B., A. P. Brooks, and D. R. Montgomery (2003), Wood in river rehabilitation  
531 and management. *The Ecology and Management of Wood in World Rivers* (eds S. V.  
532 Gregory, K.L. Boyer & A.M. Gurnell), pp. 367-389. Paper presented at Symposium 37.  
533 American Fisheries Society, Bethesda, MD.
- 534 Bennett, S. J., W. Wu, C. V. Alonso, and S. S. Wang (2008), Modeling fluvial response to  
535 in-stream woody vegetation: implications for stream corridor restoration, *Earth Surface*  
536 *Processes and Landforms*, 33(6), 890–909.
- 537 Biron, P. M., C. Robson, M. F. Lapointe, and S. J. Gaskin (2004), Comparing different  
538 methods of bed shear stress estimates in simple and complex flow fields, *Earth Surface*  
539 *Processes and Landforms*, 29(11), 1403–1415.

- 540 Brookshire, E. J., and K. A. Dwire (2003), Controls on patterns of coarse organic particle  
541 retention in headwater streams, *Journal of the North American Benthological Society*,  
542 *22*(1), 17–34.
- 543 Christiansen, C., H. Christoffersen, J. Dalsgaard, and P. Nørnberg (1981), Coastal and  
544 near-shore changes correlated with die-back in eel-grass (*Zostera Marina, L.*), *Sedimen-*  
545 *tary Geology*, *28*(3), 163–173.
- 546 Finnigan, J. (2000), Turbulence in plant canopies, *Annual Review of Fluid Mechanics*,  
547 *32*(1), 519–571.
- 548 Gacia, E., and C. M. Duarte (2001), Sediment retention by a mediterranean *Posidonia*  
549 *oceanica* Meadow: The balance between deposition and resuspension, *Estuarine, Coastal*  
550 *and Shelf Science*, *52*(4), 505–514.
- 551 García, M. (2008), *Sedimentation engineering: processes, measurements, modeling, and*  
552 *practice. 2008*, ASCE Publications.
- 553 Graf, W. H. (1984), *Hydraulics of sediment transport*, Water Resources Publication.
- 554 Hongwu, Tang and Wang, H and Liang, DF and Lv, SQ and Yan, L (2013), Incipient  
555 motion of sediment in the presence of emergent rigid vegetation, *Journal of Hydro-*  
556 *environment Research*, *7*(3), 202–208.
- 557 Inoue, M., and S. Nakano (1998), Effects of woody debris on the habitat of juvenile masu  
558 salmon (*oncorhynchus masou*) in northern japanese streams, *Freshwater Biology*, *40*(1),  
559 1–16.
- 560 Jordanova, A. A., and C. James (2003), Experimental study of bed load transport through  
561 emergent vegetation, *Journal of Hydraulic Engineering*, *129*(6), 474–478.

- 562 Kothyari, U. C., H. Hashimoto, and K. Hayashi (2009), Effect of tall vegetation on sedi-  
563 ment transport by channel flows, *Journal of Hydraulic Research*, 47(6), 700–710.
- 564 Kundu, P., and I. Cohen (2008), *Fluid Mechanics. 2004*, Elsevier Academic Press.
- 565 Lenhart, C. F. (2008), *The Influence of Watershed Hydrology and Stream Geomorphology*  
566 *on Turbidity, Sediment and Nutrients in Tributaries of the Blue Earth River, Minnesota,*  
567 *USA.*, ProQuest.
- 568 Liu, D., P. Diplas, J. Fairbanks, and C. Hodges (2008), An experimental study of flow  
569 through rigid vegetation, *Journal of Geophysical Research: Earth Surface (2003–2012)*,  
570 113(F4).
- 571 López, F., and M. H. García (2001), Mean flow and turbulence structure of open-channel  
572 flow through non-emergent vegetation, *Journal of Hydraulic Engineering*, 127(5), 392–  
573 402.
- 574 Luhar, M., J. Rominger, and H. Nepf (2008), Interaction between flow, transport and  
575 vegetation spatial structure, *Environmental Fluid Mechanics*, 8(5-6), 423–439.
- 576 Montakhab, A., B. Yusuf, A. Ghazali, and T. Mohamed (2012), Flow and sediment  
577 transport in vegetated waterways: a review, *Reviews in Environmental Science and*  
578 *Bio/Technology*, 11(3), 275–287.
- 579 Nepf, H. (1999), Drag, turbulence, and diffusion in flow through emergent vegetation,  
580 *Water resources research*, 35(2), 479–489.
- 581 Nepf, H., and E. Vivoni (2000), Flow structure in depth-limited, vegetated flow, *Journal*  
582 *of Geophysical Research: Oceans (1978–2012)*, 105(C12), 28,547–28,557.
- 583 Nepf, H. M. (2012a), Flow and transport in regions with aquatic vegetation, *Annual review*  
584 *of fluid mechanics*, 44, 123–142.

- 585 Nepf, H. M. (2012b), Hydrodynamics of vegetated channels, *Journal of Hydraulic Re-*  
586 *search*, 50(3), 262–279.
- 587 Nezu, I., and H. Nakagawa (1993), *Turbulence in open-channel flows*, Rotterdam:  
588 Balkema.
- 589 Nezu, I., and W. Rodi (1986), Open-channel flow measurements with a laser doppler  
590 anemometer, *Journal of Hydraulic Engineering*, 112(5), 335–355.
- 591 Nikora, V., F. Ballio, S. Coleman, and D. Pokrajac (2013), Spatially averaged flows  
592 over mobile rough beds: definitions, averaging theorems, and conservation equations,  
593 *Journal of Hydraulic Engineering*, 139(8), 803–811.
- 594 Nikora, V., I. McEwan, S. McLean, S. Coleman, D. Pokrajac, and R. Walters (2007),  
595 Double-averaging concept for rough-bed open-channel and overland flows: Theoretical  
596 background, *Journal of Hydraulic Engineering*, 133(8), 873–883.
- 597 Nikora, V., K. Koll, I. McEwan, S. McLean, and A. Dittrich (2004), Velocity distribution  
598 in the roughness layer of rough-bed flows, *Journal of Hydraulic Engineering*, 130(10),  
599 1036–1042.
- 600 Raupach, M., and R. Shaw (1982), Averaging procedures for flow within vegetation  
601 canopies, *Boundary-Layer Meteorology*, 22(1), 79–90.
- 602 Robbins, C. H., and A. Simon (1983), Man-induced channel adjustment in tennessee  
603 streams, *Tech. rep.*, United States Geological Survey.
- 604 Rowiński, P. M., and J. Kubrak (2002), A mixing-length model for predicting vertical  
605 velocity distribution in flows through emergent vegetation, *Hydrological sciences journal*,  
606 47(6), 893–904.

- 607 Salvador, P. G., T. Stoesser, A. Rummel, and W. Rodi (2007), Turbulent shallow flow  
608 through vegetation, *IProc. IAHR Fifth International Symposium on Environmental Hy-*  
609 *draulics (ISEH V), Arizona, USA.*
- 610 Sand-Jensen, K. (1998), Influence of submerged macrophytes on sediment composition  
611 and near-bed flow in lowland streams, *Freshwater Biology*, *39*(4), 663–679.
- 612 Schulz, M., H.-P. Kozerski, T. Pluntke, and K. Rinke (2003), The influence of macrophytes  
613 on sedimentation and nutrient retention in the lower river spree (germany), *Water*  
614 *Research*, *37*(3), 569–578.
- 615 Schulz, R., and S. K. Peall (2001), Effectiveness of a constructed wetland for retention of  
616 nonpoint-source pesticide pollution in the lourens river catchment, south africa, *Envi-*  
617 *ronmental science & technology*, *35*(2), 422–426.
- 618 Shields, F., A. Bowie, and C. Cooper (1995), Control of streambank erosion due to bed  
619 degradation with vegetation and structure1, *JAWRA Journal of the American Water*  
620 *Resources Association*, *31*(3), 475–489.
- 621 Shields Jr, F. D., N. Morin, and C. M. Cooper (2004), Large woody debris structures for  
622 sand-bed channels, *Journal of Hydraulic Engineering*, *130*(3), 208–217.
- 623 Stapleton, K., and D. Huntley (1995), Seabed stress determinations using the inertial  
624 dissipation method and the turbulent kinetic energy method, *Earth Surface Processes*  
625 *and Landforms*, *20*(9), 807–815.
- 626 Stoesser, T., S. Kim, and P. Diplas (2010), Turbulent flow through idealized emergent  
627 vegetation, *Journal of Hydraulic Engineering*, *136*(12), 1003–1017.
- 628 Tanino, Y., and H. M. Nepf (2008), Laboratory investigation of mean drag in a random  
629 array of rigid, emergent cylinders, *Journal of Hydraulic Engineering*, *134*(1), 34–41.

- 630 Warren, L. L., R. S. Wotton, G. Wharton, J. A. Bass, and J. A. Cotton (2009), The  
631 transport of fine particulate organic matter in vegetated chalk streams, *Ecohydrology*,  
632 *2*(4), 480–491.
- 633 Wilcock, P. R. (1996), Estimating local bed shear stress from velocity observations, *Water*  
634 *Resources Research*, *32*(11), 3361–3366.
- 635 Yager, E., and M. Schmeeckle (2013), The influence of vegetation on turbulence and bed  
636 load transport, *Journal of Geophysical Research: Earth Surface*, *118*(3), 1585–1601.
- 637 Yalin, M. S. (2013), *Mechanics of sediment transport*, Pergamon press.
- 638 Zong, L., and H. Nepf (2010), Flow and deposition in and around a finite patch of vege-  
639 tation, *Geomorphology*, *116*(3), 363–372.



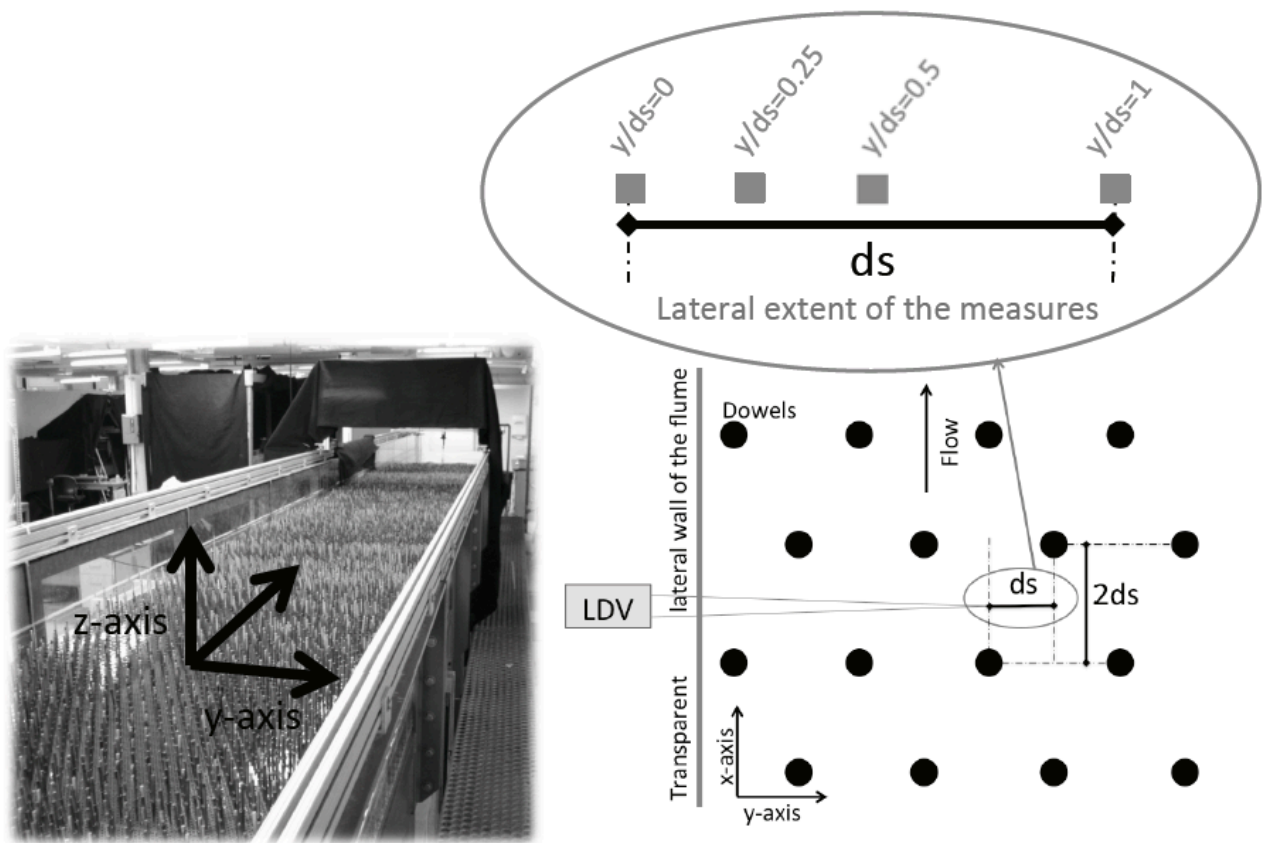


**Figure 1.** Experimental set-up. The LDV measured streamwise ( $u$ ) and vertical ( $w$ ) velocity. Vertical profiles were recorded at different lateral positions along the transect of length  $ds$  (shown above) positioned at the mid-point between two rows of wood dowels.

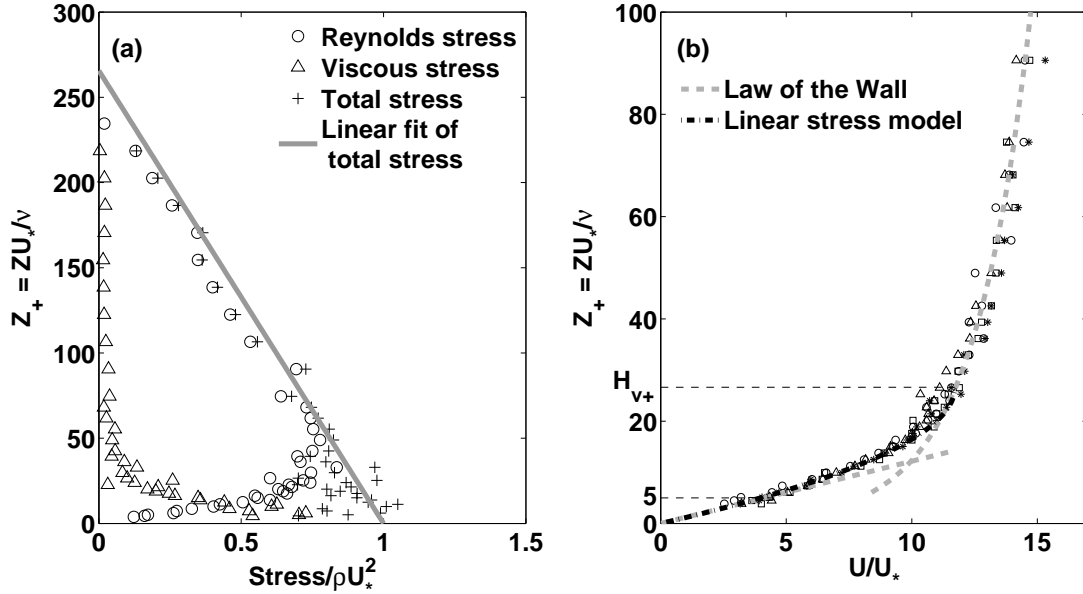


**Figure 2.** (a) Spatially-averaged stresses normalized by  $\rho U_*^2$  with  $U_*$  estimated from the total stress method, and (b) stream-wise velocity normalized by  $U_*$  at four horizontal locations (symbols) for case 1.1. The four locations are 5cm apart along a lateral transect in the middle of the flume. The near-bed viscous stress (triangles) follows a linear distribution. The linear fit to the total stress (gray solid line) represents the total stress method for  $U_*$  in Table 1. The time averaged stream-wise velocity profiles at four lateral positions are presented by four different symbols in figure (b). The velocity follows the Law of Wall (gray dashed curves in b) in the near bed region and the upper log-layer region. The new linear stress model (black dot-dash parabola) follows the measured velocity up to  $z = H_{v+} \approx 25$ .

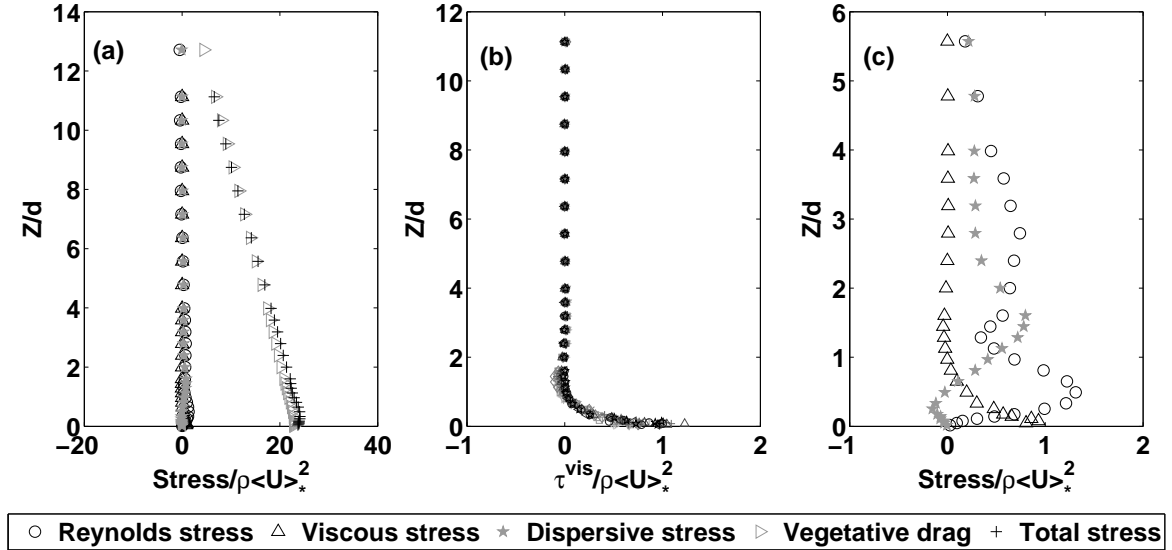


**Figure 3.** Emergent canopy case 3.1,  $a = 4.3m^{-1}$ ,  $ds = 3d$ ,  $U = 0.052m/s$ . The stem diameter for this case is  $0.0063m$ , and the fitted linear-stress layer thickness  $H_{vo} = 0.0035m$ , corresponding to  $H_{vo}/d = 0.56$ . The vertical axis is the distance from the bed normalized by the stem diameter, and the horizontal axes are the stresses normalized by  $\rho\langle U\rangle_*^2$ , the bed shear stress fitted from the spatially-averaged velocity profile. (a) The spatially averaged stress distribution is shown with the vegetative drag calculated with Eq. 5 using drag coefficients  $C_D$  estimated from a previous study by *Tanino and Nepf* [2008]. Because the total stress is dominated by vegetation drag, the total stress normalized by the bed shear stress,  $\rho\langle U\rangle_*^2$ , is much larger than 1 at the bed. (b) Viscous stress profiles measured at 11 horizontal positions (symbols). (c) Spatially averaged stresses.

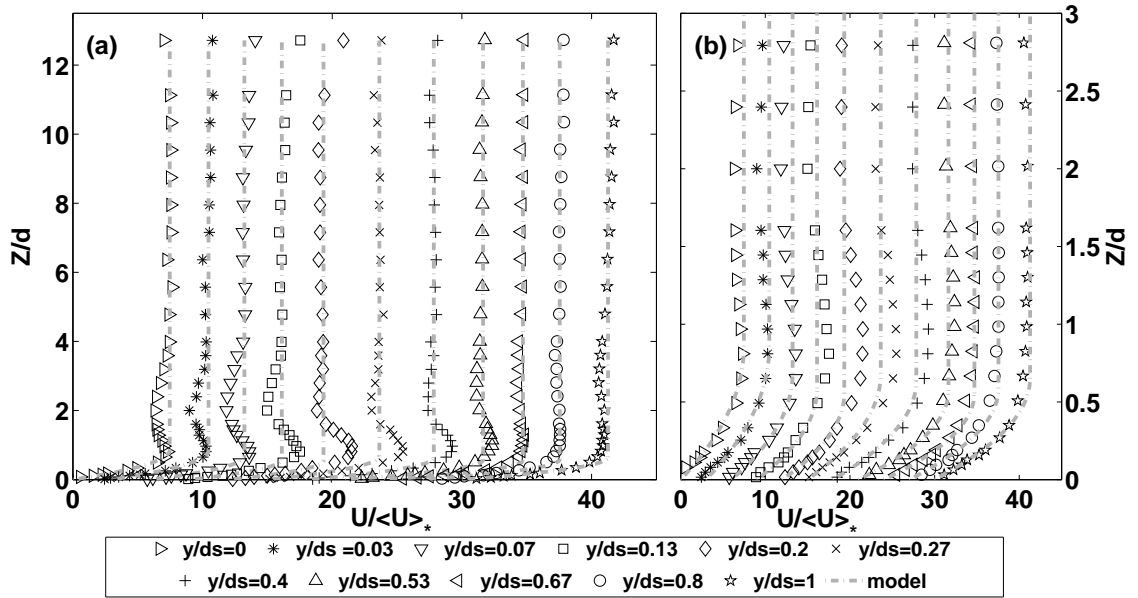


**Figure 4.** Case 3.1 (as in Fig.3). Vertical profiles of time-averaged stream-wise velocity normalized by  $\langle U \rangle_*$  at 11 horizontal positions (symbols). The  $x$ -axis of each profile is offset by 3 units. The gray dot-dash curves represent the fit of the linear-stress model (Equation 11) to each individual profile. (a) The velocity distribution over the whole water depth. In the upper layer, the velocity is vertically uniform. (b) The velocity distribution in the near bed region. The velocity is parabolic very close to the wall.

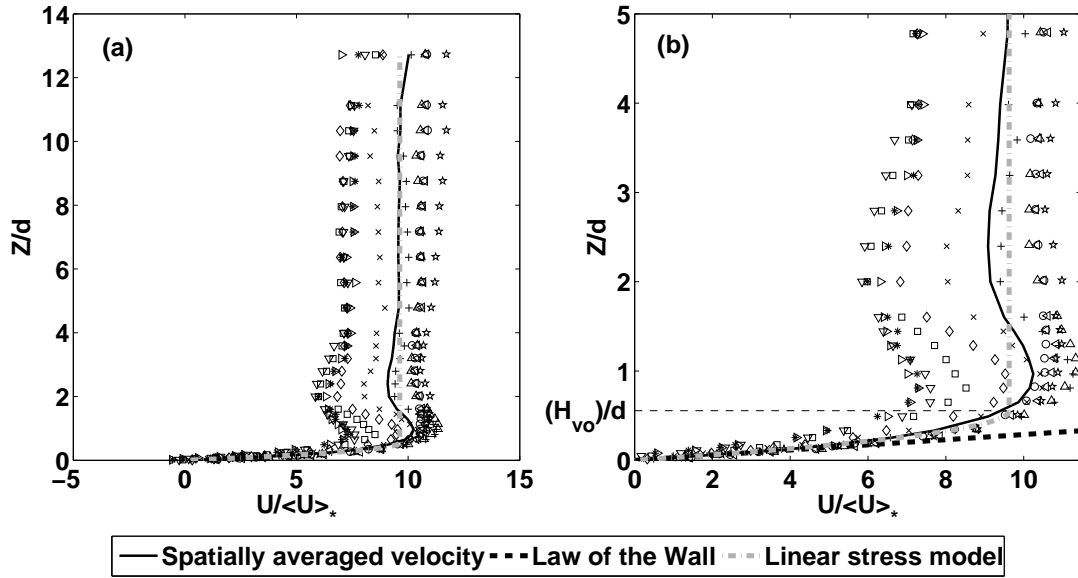


**Figure 5.** Case 3.1. Vertical profiles of time-averaged stream-wise velocity normalized by  $\langle U \rangle_*$  at 11 horizontal positions (symbols shown in Fig.4) and the spatial-average (shown with heavy black curve). The gray dot-dash curve represents the fit of the linear-stress model (Equation 11) to the spatially-averaged velocity profile. The black dashed line represents the fit of the linear part of the Law of the Wall (Equation 7) to the spatially-averaged velocity. (a) In the upper layer, the spatially-averaged velocity is constant except in regions very close to the surface. (b) The distribution of the spatially-averaged velocity in the near bed region is parabolic up to  $H_{vo}/d \approx 0.5$ .

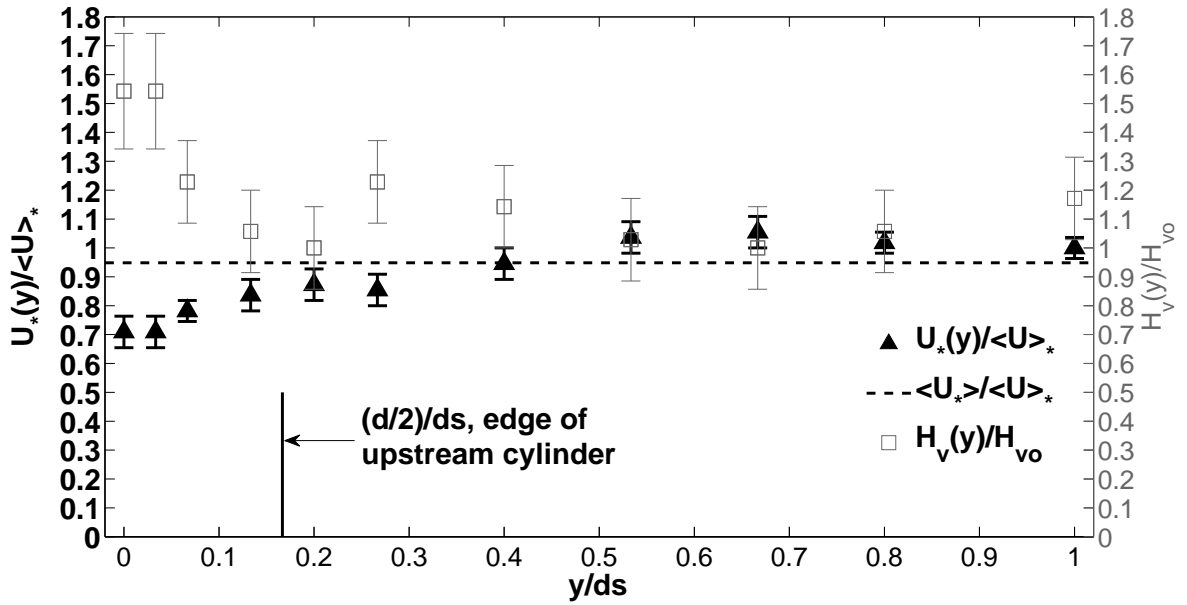


**Figure 6.** Case 3.1. The distribution of the  $U_*(y)$ , fitted from local velocity profile, normalized by  $\langle U \rangle_*$  (triangles), and the distribution of the locally fitted  $H_v(y)$  normalized by  $H_{vo}$  (squares). Here  $y$  indicates the position in the lateral transect, with  $y = 0$  right behind the dowels as shown in Fig. 1. The horizontal dashed line represents the spatial-average of local  $U_*(y)$  normalized by  $\langle U \rangle_*$ .

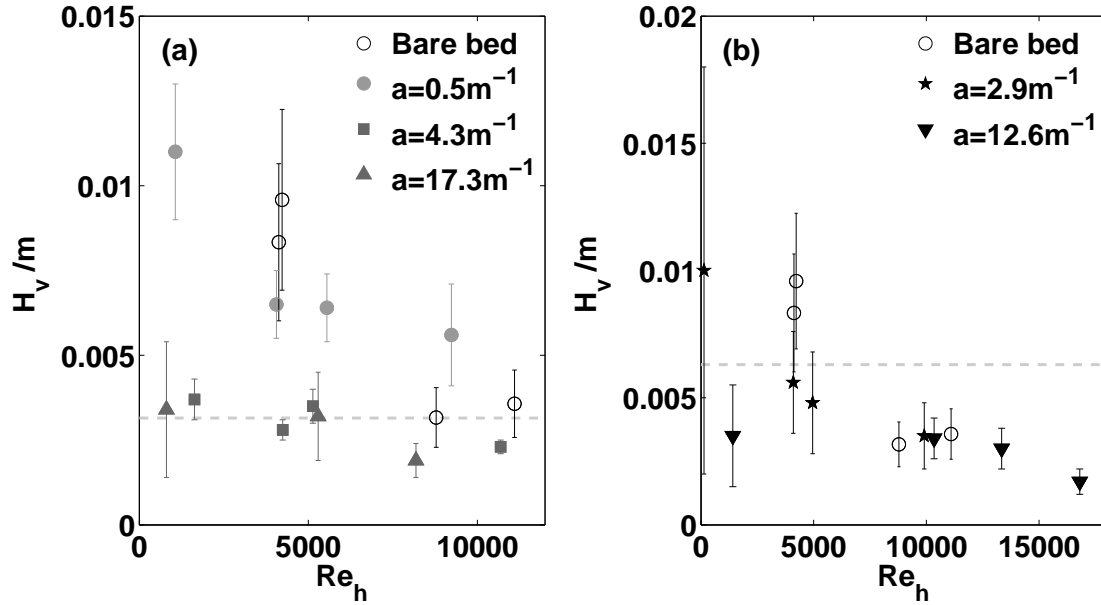


**Figure 7.** The linear-stress layer thickness,  $H_{vo}$ , versus depth Reynolds number,  $Re_H$ , for the bare channel cases (open circles) and the vegetation cases (a) with stem diameter  $d=6.3$  mm and (b) with stem diameter  $d=12.6$  mm. The depth Reynolds number  $Re_H$  is calculated using the spatially-averaged upper-layer velocity  $\langle U_o \rangle$  for the vegetated cases and the cross-sectionally-averaged velocity for the bare channel cases. The vertical error bars represent the uncertainty in fitting  $H_{vo}$ .

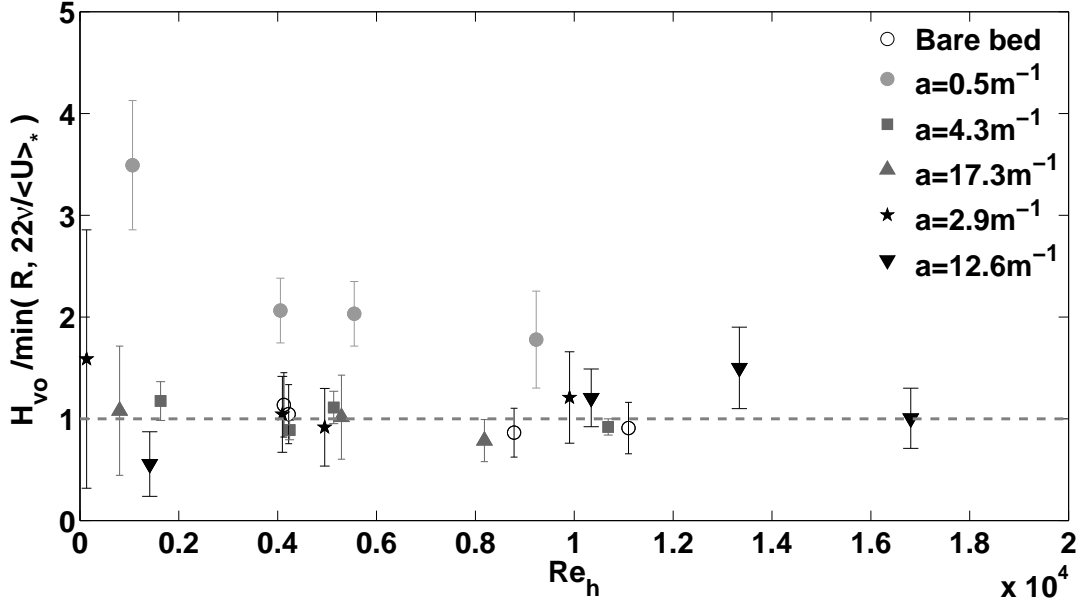


**Figure 8.** The fitted  $H_{vo}$  normalized by the proposed model  $\min(R, 22\nu / \langle U \rangle_*)$ . The dashed line indicates agreement with the proposed model. The vertical errorbars represent the fitting errors of  $H_{vo}$  normalized by  $\min(R, 22\nu / \langle U \rangle_*)$ .

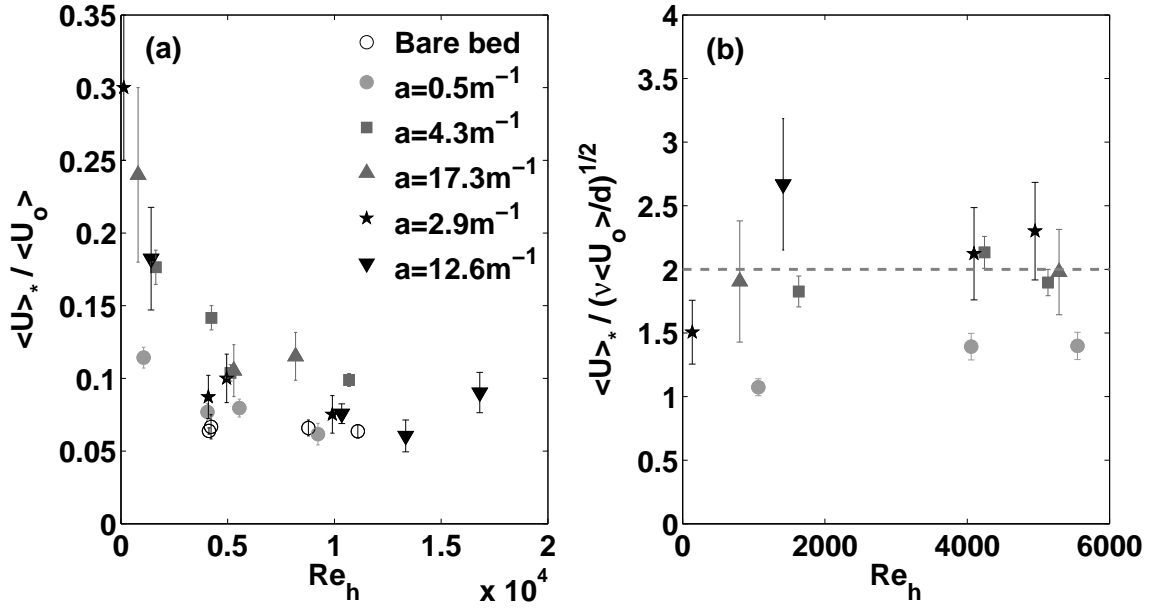


**Figure 9.** The fitted  $\langle U \rangle_*$  non-dimensionalized by (a)  $\langle U_o \rangle$  and (b)  $\sqrt{(\nu \langle U_o \rangle) / d}$ . The gray circles represent the sparse canopy ( $a = 0.5m^{-1}$ ). In the bare channel with smooth bed (open circles),  $\langle U \rangle_* / \langle U_o \rangle \approx 0.06$ .



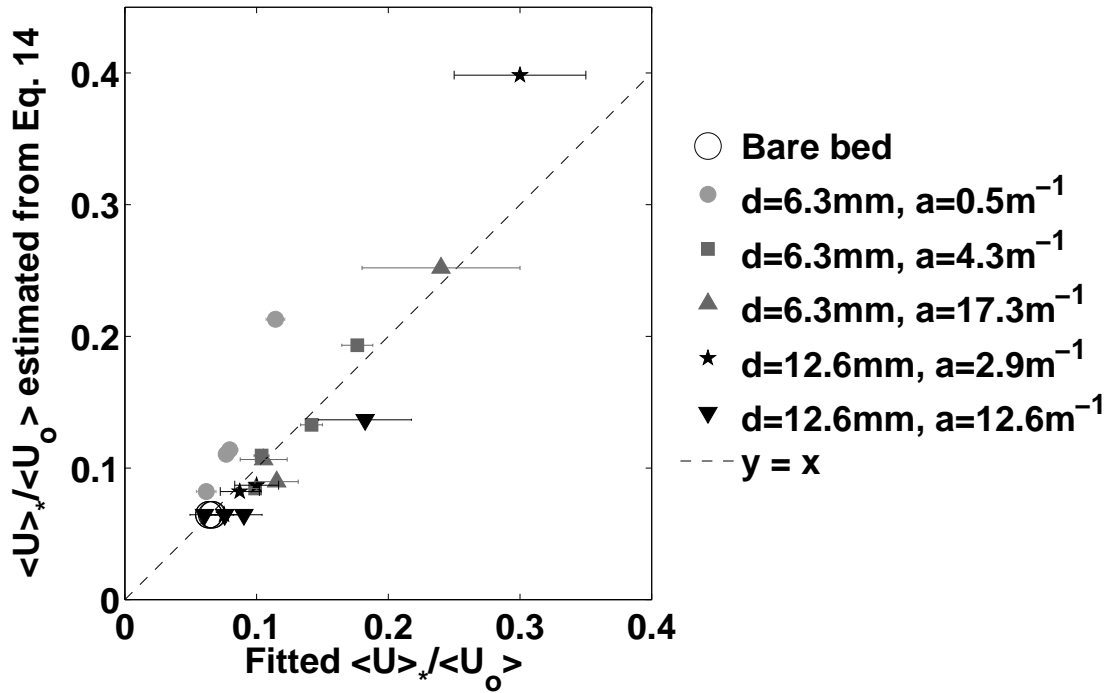


**Figure 10.**  $\langle U \rangle_*$  obtained from Eq.14 normalized by  $\langle U_o \rangle$  versus the fitted  $\langle U \rangle_*$  normalized by  $\langle U_o \rangle$ . The open circles represent bare bed value also shown in Fig.9a. The size of the open circle, however, has been enlarged to make the data more distinguishable. The uppermost data point (black pentagram) corresponds to the case with the smallest  $Re_H$  as shown in Fig.9a.

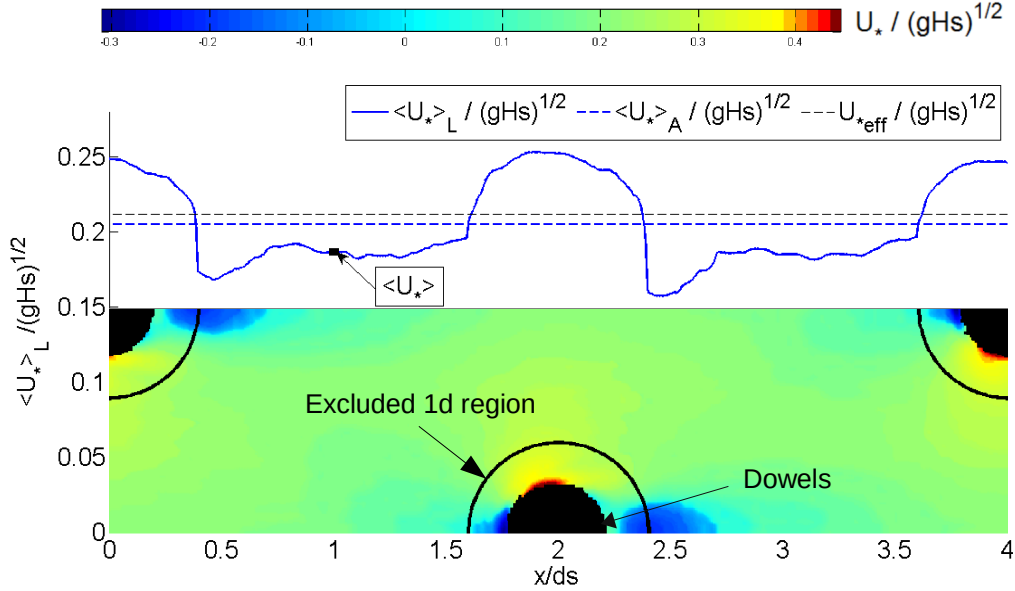


**Figure 11.** Estimates of bed shear stress normalized by the total stress,  $\sqrt{gHs}$ . Note that vegetative drag also contributes to the total stress, so that the normalized bed shear stress has an average value less than 1. The color map and color bar is adapted from Fig. 4 of [Salvador *et al.*, 2007]. In their simulation, the flow is from left to right through a staggered array of cylinders with  $ds$  (defined in Fig. 1) equal to  $2.5d$ .  $U_*$  is negative if the shear stress on the bed is in  $-x$  direction. The depth Reynolds number  $Re_H$  is around 3000. The blue curve shows the lateral-average of the simulated  $U_* / \sqrt{gHs}$  at each  $x$  position excluding 1 diameter region around the dowels. The effective friction velocity  $U_{*eff}$  is the black dashed line.

**Table 1.** Experimental conditions for 24 trials<sup>a</sup>

	Stem diameter $d[m]$	Density $a[m^{-1}]$	Spacing $ds[m]$	Average velocity $U [m/s]$	Water depth $H[m]$	Nb. of profiles (Meas. per profile)
Bare Channel						
Case 1.1	NA	0	NA	0.047	0.083	4 (40)
Case 1.2	NA	0	NA	0.091	0.094	3 (20)
Case 1.3	NA	0	NA	0.036	0.110	4 (39)
Case 1.4	NA	0	NA	0.088	0.124	3 (28)
Emergent vegetation						
Case 2.1	0.0063	0.5	0.056	0.013	0.075	11 (32)
Case 2.2	0.0063	0.5	0.056	0.093	0.098	7 (19)
Case 2.3	0.0063	0.5	0.056	0.050	0.078	9 (28)
Case 2.4	0.0063	0.5	0.056	0.048	0.114	5 (22)
Case 3.1	0.0063	4.3	0.019	0.052	0.097	11 (30)
Case 3.2	0.0063	4.3	0.019	0.083	0.120	7 (21)
Case 3.3	0.0063	4.3	0.019	0.016	0.098	5 (18)
Case 3.4	0.0063	4.3	0.019	0.036	0.117	5 (18)
Case 4.1	0.0063	17.3	0.010	0.054	0.095	7 (23)
Case 4.2	0.0063	17.3	0.010	0.010	0.082	5 (20)
Case 4.3	0.0063	17.3	0.010	0.081	0.104	7 (18)
Case 4.4	0.0063	17.3	0.010	0.047	0.111	5 (17)
Case 5.1	0.0126	2.9	0.033	0.046	0.087	5 (18)
Case 5.2	0.0126	2.9	0.033	0.099	0.098	4 (19)
Case 5.3	0.0126	2.9	0.033	0.041	0.117	4 (16)
Case 5.4	0.0126	2.9	0.033	0.002	0.075	4 (21)
Case 6.1	0.0126	12.6	0.016	0.143	0.117	9 (21)
Case 6.2	0.0126	12.6	0.016	0.098	0.100	5 (18)
Case 6.3	0.0126	12.6	0.016	0.020	0.084	6 (16)
Case 6.4	0.0126	12.6	0.016	0.176	0.074	4 (15)

<sup>a</sup> Case 4.4 has been excluded from our analysis because significant surface waves were observed in this case. The average velocity,  $U$ , is calculated as the spatial average of the individual depth-average for each profile. Due to the repeatable pattern of the dowels in  $y$  direction, the spatial-average of the depth-averaged velocity along the lateral transect shown in Fig.1 is equal to the volume flow rate per unit cross-sectional area.

**Table 2.** The friction velocity  $U_*$  estimated from three different methods<sup>b</sup>

Bare channel cases	Depth -averaged $U[m/s]$	Total stress method $U_*[m/s]$	Law of the Wall method $U_*[m/s]$	Linear-stress method	
				$U_*[m/s]$	$H_{v+} = \frac{H_v U_*}{\nu}$
Case1.1	0.047	$0.0032 \pm 0.0001$	$0.0029 \pm 0.0001$	$0.0030 \pm 0.0001$	$25 \pm 4$
Case1.2	0.091	$0.0057 \pm 0.0002$	$0.0052 \pm 0.0003$	$0.0060 \pm 0.0005$	$19 \pm 4$
Case1.3	0.036	$0.0023 \pm 0.0001$	$0.0023 \pm 0.0002$	$0.0024 \pm 0.0003$	$23 \pm 6$
Case1.4	0.088	$0.0054 \pm 0.0002$	$0.0048 \pm 0.0002$	$0.0056 \pm 0.0004$	$20 \pm 3$

<sup>b</sup>  $U_*$  estimated from three different methods agree within uncertainty. The non-dimensional linear-stress layer height  $H_{v+} = 22 \pm 3$  for the bare channel cases we studied.